

Solution of the nonlinear elasticity imaging inverse problem: the compressible case

Nachiket H Gokhale^{1,2,3}, Paul E Barbone¹ and Assad A Oberai²

¹ Department of Aerospace and Mechanical Engineering, Boston University, Boston, MA 02215, USA

² Mechanical Aerospace and Nuclear Engineering, Rensselaer Polytechnic Institute, Troy, NY 12180, USA

E-mail: gokhale@wai.com

Received 11 April 2007, in final form 21 April 2008

Published 19 June 2008

Online at stacks.iop.org/IP/24/045010

Abstract

We discuss and solve an inverse problem in nonlinear elasticity imaging in which we recover spatial distributions of hyperelastic material properties from measured displacement fields. This problem has applications to elasticity imaging of soft tissue because the strain dependence of the apparent stiffness may potentially be used to differentiate between malignant and normal tissues. We account for the geometric and material nonlinearity of the tissues by assuming a known hyperelastic model for the soft tissue. We formulate the problem as the minimization of a cost function representing the difference between the measured and predicted displacement fields. We minimize the cost function with respect to the spatial distribution of material properties using a gradient-based (quasi-Newton) optimization approach. We calculate the gradient efficiently using the adjoint method and a continuation strategy in the material properties. We present numerical examples that demonstrate the feasibility of the approach.

(Some figures in this article are in colour only in the electronic version)

1. Introduction

Elasticity imaging (EI) is an emerging medical imaging technique in which images of the spatial distribution of the elastic modulus or stiffness of soft tissues are created. The motivation and interest for pursuing this goal are numerous. For example, it is well known that pathologies affect the mechanical properties of soft tissue. This is evident in breast, prostate and other tumors presenting as hard lumps, in fibrosis which is associated with a diffuse stiffening,

³ Current address: Weidlinger Associates Inc., Applied Science Department, 375 Hudson Street, New York, NY 10014, USA.

and atherosclerosis, which means literally, hardening of the arteries [1]. There is also interest in being able to evaluate the normal properties of many tissues whose function is primarily mechanical, such as lungs, blood vessels, muscles (including cardiac muscle) and cartilage (see, for example [2]). Furthermore, there is now strong evidence that phenotypical cell behaviors depend relatively strongly on the mechanical properties of their immediate environments [3]. Finally, technological applications such as automated needle insertion [4] or surgical planning and simulation would benefit from patient-specific *a priori* or even *real-time* mechanical characterization of soft tissues.

The typical procedure followed for elasticity imaging is as follows.

- (i) *Tissue deformation and image acquisition.* The soft tissue of interest is imaged while it is deforming. The source of the deformation in general may be external (e.g. manual palpation) or internal (cardiac motion). The deformation may be quasi-static or transient [1, 5, 6].
- (ii) *Image processing.* The displacement field is calculated from the acquired images, by using either correlation-based algorithms, or minimization of a suitable objective function [7, 8].
- (iii) *Inverse problem solution.* The spatial distribution of the material properties is calculated from the known (i.e. measured) displacement field. An appropriate mathematical model for the tissue deformation is selected depending upon the spatio-temporal scales of the applied deformation and the imaging system. Given the forward mathematical model and measured deformations, an inverse problem thus follows. In this paper, we treat the inverse problem associated with a hyperelastic material model. We use an optimization formulation of the inverse problem, which we solve with an efficient adjoint and continuation algorithm.

Thus, elasticity imaging involves the solution of the following inverse problem: given the displacement field in an elastic body, calculate the spatial distribution of material properties (stiffness). Most approaches used in the literature to image the stiffness [9–15] assume that the tissue can be modeled as a linear incompressible isotropic elastic solid undergoing small-strain deformations. The goal then is to recover the shear elastic modulus distribution of the soft tissue. In this paper, we consider a *nonlinear* isotropic solid undergoing *finite* deformations. There are two expected practical advantages to using large strains in elasticity imaging. One is the potential to measure the nonlinear behavior of the tissue itself. This behavior is relevant to the physiological functioning of several tissues (e.g. arterial walls, cartilage [16]), and may also be useful in distinguishing potentially cancerous lesions [17, 18]. The second is motivated by the fact that the signal-to-noise ratio of the measured deformations tends to increase with deformation magnitude. In this case, even if the stress–strain response of the tissue remains linear over the range of strains measured, the error due to geometric nonlinearity (by this, we mean the neglect of the nonlinear terms in the exact definition of strain [19]) can become significant.

The evidence in [17, 18], for example, indicates that the degree of nonlinearity in the stress–strain relationship of breast tissue may be an indicator of the underlying histology. In [17], the mechanical properties of breast tissue samples collected from patients during surgery were measured using indentation tests at various strain levels. The authors estimated the elastic moduli at various strain levels and found that the cancerous and benign breast tissues have significant differences in the rate of increase of stiffness with strain. The authors of [18] tested the mechanical properties of both breast and prostate tissues at three different strain rates and strain levels. They also found that cancerous tissues are much stiffer at a higher strain level as compared to fat or normal glandular tissue. Both [17, 18] make their measurements

at time scales associated with quasi-static elasticity imaging (≈ 0.1 – 10 Hz), and report negligible viscoelastic effects. That is, the observed elastic modulus is independent of loading frequency.

The fact that the relative stiffness of different tissues changes with overall applied strain implies that strain contrast should change with applied strain. That potential was identified in the elasticity imaging community [20–22] and is currently being explored by several other groups. Nevertheless, the elasticity imaging literature contains relatively few attempts to quantitatively reconstruct material property distributions accounting for large deformation. Skovoroda and coworkers [23] account for geometric nonlinearities in the strain, but model soft tissue as a linear elastic incompressible material. Thus, their analysis accommodates large deformations, but assumes a linear stress–strain relation.

Measuring the nonlinear mechanical properties of soft tissues even *ex vivo* is notoriously difficult, due to practical difficulties of obtaining homogeneous samples, controlling their size and shape, and controlling the boundary conditions. To address these, several groups have turned to inverse fitting of hyperelastic models to measured force–displacement curves [21]. In these cases, the samples are assumed to have *a priori* spatially homogeneous properties.

The method presented below was developed and motivated by applications in breast imaging, with the aim of ultimately improving the detection and differential diagnosis of breast cancer. In these applications the tissue is deformed quasi-statically while it is being imaged (typically in two dimensions) with ultrasound. Image processing yields an estimate of the deformation pointwise within the tissue, at several ‘instants’ of time. The time scales of the applied deformations justify the incompressibility assumption and neglect of inertial and viscous effects [17, 18]. The deformation is typically measured in loading only, and so the pseudo-elastic [16] model is justified. We therefore assume a hyperelastic model of tissue deformation. Given the deformation field everywhere in the solid, the aim is to recover the spatial distribution (in the material or reference configuration) of the tissue properties that describe the assumed hyperelastic model.

1.1. Organization of this paper

This paper is organized as follows. We first describe the strong form of the forward hyperelastic problem in section 2. This serves to introduce our modeling assumptions, definitions and field equations. We then present the weak form which leads us to the discretization and computational solution of the forward problem. The formulation of the inverse problem follows in section 3. We formulate this as a nonlinear optimization problem. Essential to its practical solution is the efficient evaluation of the gradient. We use the adjoint method and a property continuation method to accomplish this, as described in section 4. We demonstrate the method on several examples in section 5. Among the several details discussed are the choice of hyperelastic model, the selection of the regularization constant and the effect of the magnitude of noise.

2. The forward problem

2.1. Strong form

In this section, we describe the strong form of the equations of equilibrium for a hyperelastic solid undergoing finite deformations. In this paper, this problem is referred to as the forward problem of hyperelasticity or simply as the forward problem. Given appropriate boundary data and the distribution of material properties inside the body, these equations may be solved

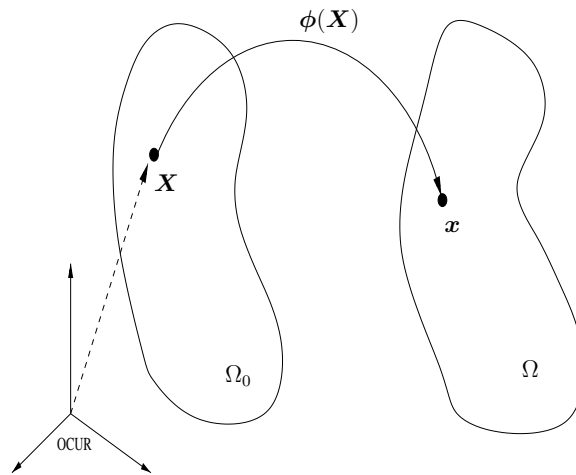


Figure 1. The deformation diagram.

to determine the deformation field $\phi(\mathbf{X})$ that maps every point \mathbf{X} in the reference or material configuration to a point \mathbf{x} in the current or spatial configuration. That is $\mathbf{x} = \phi(\mathbf{X})$ (see figure 1). The displacement field is given by $\mathbf{U}(\mathbf{X}) = \phi(\mathbf{X}) - \mathbf{X}$. For a complete treatment of this problem, the reader is referred to one of the several texts on continuum mechanics [19, 24].

The assumption of hyperelasticity implies that there exists an underlying strain energy density $W = W(\mathcal{I}; \beta)$ such that

$$\mathbf{S} = 2 \frac{\partial W}{\partial \mathbf{C}}. \quad (1)$$

In equation (1), \mathbf{C} is the right Cauchy–Green strain tensor and \mathbf{S} is the second Piola–Kirchhoff stress tensor. The Cauchy–Green strain tensor may be expressed as $\mathbf{C} = \mathbf{F}^T \mathbf{F}$, where $\mathbf{F} = \nabla^{\mathbf{X}} \phi$ is the gradient of the deformation ϕ with respect to the material coordinates. For an isotropic solid, the strain energy density W can depend on the strain tensor \mathbf{C} only through its invariants (denoted by \mathcal{I}). In addition, it is allowed to depend on a vector of material properties $\beta(\mathbf{X})$, whose values may vary spatially. The fact that the strain energy function completely characterizes the equilibrium configuration of the solid may be appreciated from the viewpoint of the principle of minimum potential energy. In relation to soft tissue mechanics, different types of mechanical behavior may be obtained by selecting different functional forms of the strain energy function W . For example, the strain energy density function for a ‘Neo–Hookean’ material is

$$W = \frac{\lambda}{4}(I_2 - 1) - \left(\frac{\lambda}{4} + \frac{\mu}{2} \right) \ln I_2 + \frac{\mu}{2}(I_1 - 2). \quad (2)$$

Here, λ and μ are material parameters. In the limit of infinitesimal deformations they can be interpreted as the Lamé parameters. We discuss this and another strain energy density function in section 5, where the corresponding Piola–Kirchhoff and material tangent modulus tensors are also derived.

The equations of equilibrium in the absence of body forces may be written in the reference configuration, Ω_0 , as

$$\nabla^{\mathbf{X}} \cdot (\mathbf{F}\mathbf{S}) = \mathbf{0} \quad \text{in } \Omega_0 \quad (3)$$

$$\mathbf{U} = \mathbf{G} \quad \text{on } \Gamma_G \quad (4)$$

$$\mathbf{FS} \cdot \mathbf{N} = \mathbf{H} \quad \text{on } \Gamma_H. \quad (5)$$

In equations (3)–(5), Γ_G and Γ_H are subsets of the boundary $\{\Gamma_0 = \partial\Omega_0\}$ on which displacement and traction boundary data, \mathbf{G} and \mathbf{H} , respectively, are specified. Γ_0 denotes the boundary of Ω_0 . Note that $\Gamma_0 = \Gamma_G \cup \Gamma_H$ and $\Gamma_G \cap \Gamma_H = \emptyset$, that is, either displacement or traction boundary conditions must be specified on the entire boundary. In equation (5), \mathbf{N} denotes a unit outward normal vector in the reference configuration. With this background about the strong form of the equilibrium equations, we proceed to the weak form of these equations and their computational solution. For a detailed description of the material the reader is referred to [25].

2.2. The weak form and its numerical solution

We begin by defining function spaces \mathcal{S} and \mathcal{V} , for admissible solutions and weighting functions, respectively:

$$\mathcal{S} = \{\mathbf{U} | U_i \in H^1(\Omega_0); U_i = G_i \text{ on } \Gamma_G\} \quad (6)$$

$$\mathcal{V} = \{\mathbf{V} | V_i \in H^1(\Omega_0); V_i = 0 \text{ on } \Gamma_G\}. \quad (7)$$

Note that both spaces are subsets of H^1 , the Sobolev space of square integrable functions with square integrable derivatives. Functions in \mathcal{S} satisfy the Dirichlet boundary condition, while functions in \mathcal{V} satisfy its homogeneous counterpart.

The weak formulation of the equilibrium equations (3)–(5) can be obtained by multiplying equation (3) by a weighting function $\mathbf{W} \in \mathcal{V}$ and integrating by parts. Alternatively it may be obtained directly by minimizing the total potential energy of the system. In the reference configuration the weak form is given by: find a displacement field $\mathbf{U} \in \mathcal{S}$ such that

$$\mathcal{A}(\mathbf{W}, \mathbf{U}; \beta) - \int_{\Gamma_H} \mathbf{W} \cdot \mathbf{H} \, d\Gamma_0 = 0, \quad \forall \mathbf{W} \in \mathcal{V}, \quad (8)$$

where the semi-linear form $\mathcal{A}(\cdot, \cdot; \beta)$ is given by

$$\mathcal{A}(\mathbf{W}, \mathbf{U}; \beta) = \int_{\Omega_0} W_{k,I} F_{k,J} S_{JI} \, d\Omega_0. \quad (9)$$

Note that the dependence of \mathcal{A} on the material properties is through the definition of the stress tensor given in equation (1).

In the equations above and throughout this paper, repeated indices in the subscript imply summation from one to the number of spatial dimensions. A subscript following a comma denotes a derivative along that material coordinate direction. That is $(\cdot)_{,I} = \frac{\partial(\cdot)}{\partial X_I}$.

The weak form may be approximated using Galerkin's method in conjunction with standard finite element basis functions to obtain an approximate numerical solution of the forward problem. This solution requires the linearization of the semilinear form \mathcal{A} , about an arbitrary displacement field state \mathbf{U} which yields a bilinear form \mathcal{B} given by

$$\begin{aligned} \mathcal{B}(\mathbf{W}, \Delta\mathbf{U}; \beta, \mathbf{U}) &= \left. \frac{d}{d\epsilon} \right|_{\epsilon \rightarrow 0} \mathcal{A}(\mathbf{W}, \mathbf{U} + \epsilon \Delta\mathbf{U}; \beta) \\ &= \int_{\Omega_0} W_{m,J} (\delta_{mn} S_{JL} + F_{mI} F_{nK} \mathbb{C}_{IJKL}) \Delta U_{n,L} \, d\Omega_0. \end{aligned} \quad (10)$$

In equation (10), \mathbb{C}_{IJKL} are the components of the fourth-order material tangent tensor, given by

$$\mathbb{C}_{IJKL} = 2 \frac{\partial S_{IJ}}{\partial C_{KL}} = 4 \frac{\partial^2 W}{\partial C_{IJ} \partial C_{KL}}. \quad (11)$$

It is clear from equation (11) that this tensor possesses major symmetry, that is $\mathbb{C}_{IJKL} = \mathbb{C}_{KLIJ}$. In addition, due to the symmetry of \mathbf{C} and \mathbf{S} this tensor possesses minor symmetries, that is $\mathbb{C}_{IJKL} = \mathbb{C}_{IJLK} = \mathbb{C}_{JIKL}$. Using these properties it may be verified from (10) that $\mathcal{B}(\cdot, \cdot; \beta, \mathbf{U})$ is symmetric.

2.3. Numerical solution

The equations of equilibrium for a solid undergoing finite deformations are significantly harder to solve than their linear, infinitesimal deformation counterparts. The former lead to a set of nonlinear algebraic equations that may not converge for large applied loads. To overcome this problem, an incremental loading strategy is often adopted. It may be thought of as a path following or continuation method in the loading parameter. Though this is standard treatment in the solid mechanics community, we describe it briefly here to contrast it with our nonstandard continuation strategy described in section 4.2.

For simplicity of presentation, suppose $\mathcal{S} = \mathcal{V}$ (i.e. all Dirichlet boundary conditions are homogeneous). We let $0 \leq L \leq 1$ denote a loading parameter, such that $L = 0$ corresponds to zero loading of the body, and $L = 1$ corresponds to full loading. Thus we may regard the displacement field $\mathbf{U} \equiv \mathbf{U}(\mathbf{X}; \beta, L)$ to be a function of L , such that equation (8) becomes

$$\mathcal{A}(\mathbf{W}, \mathbf{U}(\beta, L); \beta) - L \int_{\Gamma_H} \mathbf{W} \cdot \mathbf{H} \, d\Gamma_0 = 0, \quad \forall \mathbf{W} \in \mathcal{V}. \quad (12)$$

We note that at zero loading, $\mathbf{U}(\mathbf{X}; \beta, 0) = \mathbf{0}$. Now we suppose that we know $\mathbf{U}(L - \Delta L)$ and seek to find $\mathbf{U}(L)$. This motivates the following Newton iteration:

$$\mathbf{U}^{(0)}(\mathbf{X}; \beta, L) = \mathbf{U}(\mathbf{X}; \beta, L - \Delta L) \quad (13)$$

$$\mathcal{B}(\mathbf{W}, \Delta \mathbf{U}^{(i)}; \beta, \mathbf{U}^{(i)}) = L \int_{\Gamma_H} \mathbf{W} \cdot \mathbf{H} \, d\Gamma_0 - \mathcal{A}(\mathbf{W}, \mathbf{U}^{(i)}; \beta), \quad \forall \mathbf{W} \in \mathcal{V}. \quad (14)$$

$$\mathbf{U}^{(i+1)}(\mathbf{X}; \beta, L) = \mathbf{U}^{(i)}(\mathbf{X}; \beta, L) + \Delta \mathbf{U}^{(i)}(\mathbf{X}). \quad (15)$$

Each Newton iteration is tantamount to solving an anisotropic linear elasticity problem. In the discrete context, for sufficiently small ΔL , the Newton iterations converge; for large ΔL , the Newton iterations diverge. This dictates that typically several loading steps (n_{load}) are required to reach the full loading, $L = 1$. In our applications, we have found that $n_{\text{load}} \approx 80$, and that we require about $n_{\text{Newton}} \approx 6$ iterations at each load step. Thus the effort of solving the forward nonlinear elasticity problem is roughly 500 times the effort of solving the forward linear elasticity problem. Further, since solving the inverse hyperelasticity problem requires a series of forward solves, it is imperative that the time taken to solve the forward problem be kept within a manageable limit. In section 4.2 we describe an approach that accomplishes this.

3. Formulation of the inverse problem

We formulate the inverse problem as a constrained minimization problem and solve it using a quasi-Newton optimization algorithm (BFGS). These types of algorithms require the gradient of the objective function with respect to the optimization parameters at every iteration. The gradient is evaluated efficiently using the adjoint of the linearized hyperelasticity equations. The cost of evaluating the gradient would otherwise dominate the overall cost of solving the inverse problem, and the use of adjoint equations helps us to keep this cost in check. Further it ensures that the cost of the gradient calculation does not grow as the number of optimization

parameters increases. Similar approaches for solving inverse problems have been used in other application areas [12, 26–28].

We consider a generic hyperelastic material model which depends on a vector of N_β material properties, $\beta = [\beta_1, \dots, \beta_{N_\beta}]^T$, where each property is allowed to vary spatially. We seek the spatial distribution of material properties which minimizes the difference between a set of $\{N_{\text{meas}}\}$ measured displacement fields $U^1_{\text{meas}}, \dots, U^{N_{\text{meas}}}_{\text{meas}}$ and the corresponding set of predicted displacement fields $U^1, \dots, U^{N_{\text{meas}}}$. The predicted displacement fields are constrained to satisfy the equations of equilibrium. The objective function is the square of the L_2 norm of the difference between the measured and predicted displacement fields. We have chosen the L_2 norm (as opposed to H^1 norm for instance) as it avoids the differentiation of a noisy measured displacement field. Further if the noise in the measured displacement fields is Gaussian it yields a maximum likelihood estimate of the material properties [29, pp 657–8].

The statement of the inverse problem is: find the spatial distribution of the material properties $\beta(\mathbf{X})$ that minimizes the objective function π given by

$$\pi = \frac{1}{2} \sum_{n=1}^{N_{\text{meas}}} w_n \|\mathbf{T}(U^n) - \mathbf{T}(U^n_{\text{meas}})\|_0^2 + \frac{1}{2} \sum_{j=1}^{N_\beta} \alpha_j \rho(\beta_j), \quad (16)$$

subject to the constraint that each predicted deformation field U^n satisfies the equilibrium equations (1)–(5), or (8) and (1).

In the above equation, U^n_{meas} is the measured displacement field corresponding to the n th measurement, U^n is the corresponding predicted displacement field for the n th measurement, \mathbf{T} is a tensor that weights the appropriate displacement components, $\|\cdot\|_0$ denotes the L_2 norm and w_n represents a weighting factor. In addition, for each material property field β_j , α_j is a regularization parameter and ρ is the regularization functional. The significance of these quantities is discussed below.

Weighting factors. The weighting factors w_n are chosen so that all measurements contribute equally to the objective function π . This helps control bias toward measurements with large deformation. For example, suppose two measurements were available and one of these, say the second, contained much larger displacements. Then the objective function would be more sensitive to the second field, and the minimization algorithm would be biased in favor of minimizing this field. In order to remove this bias, it may be useful to select the weights to be inversely proportional to a measure of magnitude of the displacement fields. That is

$$w_1 = \left(\frac{q_2}{q_1}\right)^2 \quad \text{and} \quad w_2 = 1, \quad (17)$$

where q_1, q_2 represent the magnitudes of the measured displacements.

Measurement tensor. Imaging systems often have anisotropic resolution and thus provide more accurate displacement measurements in some directions than in others. The tensor \mathbf{T} can be used to emphasize the accurate components of displacement over the others. For example, in ultrasound, the axial displacement component (say in the direction of the unit vector e_2) is so much more accurate than the other displacement components that the latter are frequently discarded. In this situation, an appropriate choice for \mathbf{T} would be

$$\mathbf{T} = e_2 \otimes e_2. \quad (18)$$

The regularization term. In equation (16) α_j is a regularization factor, which controls the tradeoff between matching the predicted and measured displacement fields and certain *a priori* assumed physical characteristics of the spatial distributions of the material properties

(such as smoothness). These characteristics are selected through an appropriate choice of the regularization functional denoted by $\rho(\cdot)$. The choice of L_2 norm, given in (19), ensures that the material property distribution does not attain unphysically large values. The H^1 semi-norm, defined in equation (19), penalizes oscillations in the solution, and ensures smoothness of the recovered material property distributions. The total variation diminishing (TVD) regularization does just that, but does not penalize the steepness of jumps in the solution. This makes it well suited to the task of capturing solutions with discontinuities. We implement a regularized TVD regularization, defined in equation (19). It contains a small parameter c that ensures differentiability of the regularization functional at $|\nabla\beta_j| = 0$. In this paper, we present results with the regularized TVD regularization and have chosen $c = 0.1$:

$$\rho(\beta_j) = \begin{cases} \int_{\Omega_0} \beta_j^2 \, d\Omega_0 & (L_2 \text{ norm}) \\ \int_{\Omega_0} |\nabla\beta_j|^2 \, d\Omega_0 & (H_1 \text{ semi-norm}) \\ \int_{\Omega_0} \sqrt{|\nabla\beta_j|^2 + c^2} \, d\Omega_0 & (\text{regularized TVD}). \end{cases} \quad (19)$$

4. Inverse problem solution using the adjoint method

In the previous section we have formulated the inverse hyperelasticity problem as a constrained minimization problem. To solve this problem we rely on a quasi-Newton algorithm which requires the gradient vector at each iteration. We now present a method to evaluate the gradient efficiently which makes use of the adjoint elasticity equations and a continuation strategy in material parameters.

4.1. Gradient calculation via the adjoint method

We note that in the objective function π (see (16)), each predicted displacement field U^n depends on β through the equilibrium equations (1) and (8), which it is constrained to satisfy. In this section, we will derive an expression for the derivative of the objective function with respect to the material properties in a given arbitrary direction $\delta\beta$. This expression will lead us to an expression for the gradient.

We denote the variation of a function $f(x)$ in the direction δx by δf ,

$$\delta f = D_x f \cdot \delta x = \left. \frac{d}{d\epsilon} \right|_{\epsilon \rightarrow 0} f(x + \epsilon \delta x). \quad (20)$$

Here, $D_x f$ is the directional derivative of the function $f(x)$. For example, changing the material properties from β to $\beta + \delta\beta$ causes the predicted displacement field to change from U^n to $U^n + \delta U^n$, where

$$\delta U^n = D_\beta U^n \cdot \delta\beta. \quad (21)$$

With δU^n defined above, we may now differentiate π (equation (16)) to obtain

$$\delta\pi = \sum_{n=1}^{N_{\text{meas}}} w_n (\mathbf{T}(\delta U^n), \mathbf{T}(U^n - U^n_{\text{meas}})) + \sum_{j=1}^{N_\beta} \alpha_j \mathcal{R}(\delta\beta_j, \beta_j). \quad (22)$$

The second term in (22) is the derivative of the regularization functional $\rho(\cdot)$; it may be evaluated directly. The first term, on the other hand, is quite challenging to evaluate because it involves δU^n . The equation for δU^n is obtained by differentiating constraint (8) with respect to β . This gives

$$\mathcal{B}(W^n, \delta U^n; \beta, U^n) + \mathcal{C}(W^n, \delta\beta; \beta, U^n) = 0 \quad \forall W^n \in \mathcal{V}. \quad (23)$$

Here there is no sum on n and $n = 1 \cdots n_{\text{meas}}$. We recall that $\mathcal{B}(\cdot, \cdot; \cdot, \cdot)$ is defined in equation (10). It represents the derivative of $\mathcal{A}(\cdot, \cdot; \beta)$ with respect to U . The bilinear form $\mathcal{C}(\cdot, \cdot; \beta, U^n)$ is bilinear in its first two arguments, and represents the explicit derivative of $\mathcal{A}(\cdot, \cdot, \beta)$ with respect to β . It is given by

$$\mathcal{C}(\mathbf{W}^n, \delta\beta; \beta, U^n) = \int_{\Omega_0} W_{k,l}^n F_{k,J}^n (\mathbf{D}_\beta S_{IJ}^n \cdot \delta\beta) d\Omega_0. \quad (24)$$

Equation (23) determines δU^n in terms of $\delta\beta$. One approach to evaluating the derivative of π in a particular direction would be as follows. Given a particular choice for $\delta\beta$, we may solve (23) for δU^n . We then utilize this value in (22) to determine $\delta\pi$. In order to evaluate the entire gradient, we sequentially choose different directions and repeat the process. This approach is clearly inefficient, however, because it requires a linear elasticity solution for *each* direction in $\delta\beta$.

As an alternative, we can use the adjoint equation to express explicitly the δU^n contribution to $\delta\pi$. To that end, we consider (23) and look for the condition when the δU^n term in this equation will be equal to the δU^n term in (22). We recognize that this will hold for a specific choice for the weighting function in (23). This function is $\overline{\mathbf{W}}^n \in \mathcal{V}$, that is the solution of the following adjoint boundary value problem:

$$\mathcal{B}(\overline{\mathbf{W}}^n, \mathbf{V}; \beta, U^n) + (\mathbf{T}\mathbf{V}, \mathbf{T}(U^n - U_{\text{meas}}^n)) = 0 \quad \forall \mathbf{V} \in \mathcal{V}. \quad (25)$$

Equation (25) is the ‘adjoint equation’. In (25) the function $\mathbf{V} \in \mathcal{V}$ is an arbitrary weighting function. The function $\overline{\mathbf{W}}^n$, on the other hand, is not arbitrary. It is the solution of (25) and as such is analogous to a Lagrange multiplier; it is in the weighting space, \mathcal{V} , but it is not an arbitrary weighting function. We note that the reversal of roles (i.e. the slots in \mathcal{B}) of the weighting functions in (23) and (25) motivates calling (23) the adjoint equation. In this particular case, \mathcal{B} is symmetric and the operator is self-adjoint.

To eliminate the δU^n from our expression for $\delta\pi$ we note that (23) holds for all $\mathbf{W}^n \in \mathcal{V}$. In particular, it holds for $\mathbf{W}_n \leftarrow \overline{\mathbf{W}}^n$. Similarly, (25) holds for all $\mathbf{V} \in \mathcal{V}$, and in particular holds for $\mathbf{V} \leftarrow \delta U^n \in \mathcal{V}$. Making these substitutions and subtracting the resulting equations gives

$$(\mathbf{T}(\delta U^n), \mathbf{T}(U^n - U_{\text{meas}}^n)) - \mathcal{C}(\overline{\mathbf{W}}^n, \delta\beta; \beta, U^n) = 0. \quad (26)$$

We thus get our final expression for the gradient by using (26) in (22) to write

$$\delta\pi = \sum_{n=1}^{N_{\text{meas}}} w_n \mathcal{C}(\overline{\mathbf{W}}^n, \delta\beta; \beta, U^n) + \sum_{j=1}^{N_\beta} \alpha_j \mathcal{R}(\delta\beta_j, \beta_j). \quad (27)$$

Equation (27) represents the change in π due to an infinitesimal change in the material properties in the direction of $\delta\beta$. It is now expressed explicitly in terms of $\delta\beta$. It also involves a new field, the adjoint field $\overline{\mathbf{W}}^n$, which is obtained by solving (25).

To derive an expression for the gradient for the finite dimensional problem, we expand the material properties in terms of a basis,

$$\beta_j = \sum_{A=1}^{N_{\text{props}}} M_A(\mathbf{X}) b_{jA}. \quad (28)$$

In the above equation, N_{props} represents the number of basis functions, $M_A(\mathbf{X})$, used to represent each material property and b_{jA} is the coefficient of the j th material property corresponding to the A th basis function. Variations in the material properties, $\delta\beta = \delta\beta_j e_j$, are given by

$$\delta\beta_j = \sum_{A=1}^{N_{\text{props}}} M_A(\mathbf{X}) \delta b_{jA}, \quad (29)$$

where δb_{jA} represent variations in b_{jA} and e_j is a vector with 1 in the j th location and 0 elsewhere. Using (29) in (27) gives

$$\delta\pi = \sum_{j=1}^{N_\beta} \sum_{A=1}^{N_{\text{props}}} g_{jA} \delta b_{jA}, \quad (30)$$

where g_{jA} is identified as the gradient of π with respect to the A th coefficient of the j th material property. From (27)–(30) we conclude

$$g_{jA} = \sum_{n=1}^{N_{\text{meas}}} w_n \mathcal{C}(\overline{\mathbf{W}}^n, M_A e_j; \beta, \mathbf{U}^n) + \alpha_j \mathcal{R}(\beta_j, M_A). \quad (31)$$

This is our final expression for the gradient. In order to evaluate g_{jA} using this expression, we first solve N_{meas} nonlinear forward problems given by (8) to determine $\mathbf{U}^1, \dots, \mathbf{U}^{N_{\text{meas}}}$; we then solve N_{meas} linear adjoint problems (25) to determine $\overline{\mathbf{W}}^1, \dots, \overline{\mathbf{W}}^{N_{\text{meas}}}$; we use these results in (31) to evaluate the gradient. The gradient thus calculated is used to perform a BFGS update to the material properties. Our overall algorithm to solve the inverse problem is described in figure 1.

Algorithm 1. Solution of the hyperelasticity inverse problem

- 1 : Start with a homogeneous distribution of material properties $\beta_1(\mathbf{X}), \beta_2(\mathbf{X}), \dots, \beta_{N_\beta}(\mathbf{X})$
 - 2 : **repeat**
 - 3 : Solve forward hyperelasticity problems with the current distribution of the material properties using the previous displacement field if available
 - 4 : Solve corresponding linear adjoint problems
 - 5 : Evaluate the objective function and its gradient
 - 6 : Use these in quasi-Newton update for the material properties
 - 7 : **until** Either the objective function π is low enough or the maximum number of iterations have been reached.
-

Remarks

- (i) In order to evaluate the gradient, the adjoint method requires as many solves of the forward hyperelasticity and adjoint problems as the number of measured displacement fields. This number is *independent of the total number of discrete variables used to represent the material properties*, that is, it is independent of both the number of material properties, N_β , and the number of variables used to represent each property, N_{props} . In a typical application we expect two to four measured displacement fields, however we would expect $N_\beta = 2$ material properties and about $N_{\text{props}} = 1600$ (a grid of $\approx 40 \times 40$) variables to represent each property, leading to about 3200 material variables. Hence it is a significant advantage that the number of solves in the proposed algorithm is independent of the total number of material variables.
- (ii) We have not addressed the uniqueness of the inverse hyperelasticity problem. Indeed, there could be more than one set of material property distributions, perhaps even entire families, that could minimize the objective function in (16). For the corresponding inverse problem in the linear, infinitesimal deformation case, it has been shown that the uniqueness of the solution depends on the boundary conditions. For instance it is known that for plane strain problems with prescribed displacement boundary conditions, a single

measured displacement field is not sufficient to ensure uniqueness [30, 31]. In plane stress, on the other hand, a single displacement field is sufficient to determine the shear modulus in an incompressible material. In the hyperelastic case with nonlinear material behavior, we expect these trends to carry over. We use boundary conditions that would give a unique reconstruction in the corresponding linear problem. It is clear, however, that we require more information to recover multiple material properties than for one material property.

- (iii) The inequalities of Baker–Ericksen, Coleman–Noll, and strong ellipticity need to be satisfied for each estimate of the material properties in the inversion algorithm. These inequalities are motivated by physical considerations such as ‘stress increases with strain’ and require certain constraints to hold among the material properties appearing in the hyperelastic relation. Violating these inequalities may lead to problems of convergence in the finite element method and material models with unphysical behavior. The reader is referred to [24] for a discussion of these concepts. For the constitutive models considered in our study, these inequalities are satisfied by enforcing positivity constraints on the variables.

4.2. Continuation in material properties

Each iteration of the inverse solution requires an evaluation of the gradient. Each gradient calculation with the adjoint method requires N_{meas} nonlinear forward solutions, and N_{meas} (linear) adjoint solutions. The nonlinear forward solution dominates the computational cost. A naive estimate of the cost based on the discussion in section 2.3 would be several hundred times the cost of the inverse linear elastic problem. Here we describe a continuation method in the material properties that reduces this to five to ten times the cost of the inverse linear elastic problem.

After each iteration of the inverse problem, we get an update to the material properties. We need then to re-solve the nonlinear hyperelastic problem for this new set of parameters. Here we recognize that $U(\mathbf{X}; \beta, L)$ depends upon β and focus on that dependence; we shall therefore suppress the other arguments of $U(\beta)$. We denote by β_1 the current guess of the material property distributions, and by β_2 the new guess of material properties from the optimization algorithm. We suppose that we know $U(\beta_1)$ that satisfies (8) and we seek $U(\beta_2)$ that satisfies

$$\mathcal{A}(\mathbf{W}, U(\beta_2); \beta_2) - \int_{\Gamma_H} \mathbf{W} \cdot \mathbf{H} \, d\Gamma_0 = 0, \quad \forall \mathbf{W} \in \mathcal{V}. \quad (32)$$

Rather than solving (32) by continuation in the loading parameter from $L = 0$ with material properties fixed at β_2 , we instead fix $L = 1$ and use continuation in the material properties. To that end, we introduce a parameter $0 \leq \lambda \leq 1$, and let

$$\beta(\lambda) = (1 - \lambda)\beta_1 + \lambda\beta_2 \quad (33)$$

$$\Delta\beta = \Delta\lambda(\beta_2 - \beta_1). \quad (34)$$

That leads us to the following Newton iteration:

$$U^{(0)}(\mathbf{X}; \beta(\lambda + \Delta\lambda)) = U(\mathbf{X}; \beta(\lambda)) \quad (35)$$

$$\begin{aligned} \mathcal{B}(\mathbf{W}, \Delta U^{(i)}; \beta(\lambda + \Delta\lambda), U^{(i)}) &= \int_{\Gamma_H} \mathbf{W} \cdot \mathbf{H} \, d\Gamma_0 \\ &\quad - \mathcal{A}(\mathbf{W}, U^{(i)}; \beta(\lambda + \Delta\lambda)), \quad \forall \mathbf{W} \in \mathcal{V} \end{aligned} \quad (36)$$

$$U^{(i+1)}(\mathbf{X}; \beta(\lambda + \Delta\lambda)) = U^{(i)}(\mathbf{X}; \beta(\lambda + \Delta\lambda)) + \Delta U^{(i)}(\mathbf{X}). \quad (37)$$

As with continuation in the loading parameter, the Newton iterations will converge for sufficiently small $\Delta\lambda$. In all the examples we present later, the Newton iterations converge for $\Delta\lambda = 1$, i.e. the full material property update. Thus we get the full nonlinear hyperelastic solution for the new material properties in a total of about six Newton iterations. In situations where the material property update is not small enough for the Newton iterations to converge directly, the full update may need to be applied in several ‘material steps’ with $\Delta\lambda < 1$.

4.3. Computational costs of the overall strategy

In the proposed approach, we solve the nonlinear forward problem at each step of the optimization algorithm. During the first step this involves continuation in the load parameter, incrementing it in n_{load} steps while performing n_{Newton} iterations at each load step. For problems with strains of up to 20%, $n_{\text{load}} \approx 100$, and $n_{\text{Newton}} \approx 6$. Thereafter, during every subsequent step of the optimization algorithm, we solve the nonlinear forward problem by employing continuation in the material parameter and not the load parameter. We utilize the solution of the fully loaded state from previous optimization step (and material property state) and perform n_{Newton} iterations to converge to the solution for the new material property state. Thus the cost of a nonlinear forward solve reduces to n_{Newton} linear solves from $n_{\text{load}} \times n_{\text{Newton}}$ linear solves. This material continuation is utilized for a total of $n_{\text{opt}} - 1$ optimization steps, where n_{opt} is the total number of optimization steps. Based on this strategy the total cost of solving the inverse problem with one measured displacement field is approximately $(n_{\text{load}} + n_{\text{opt}} - 1) \times n_{\text{Newton}} + n_{\text{opt}}$ linear solves. In this expression, the first term represents the cost associated with solving the nonlinear forward problem and the second term is the cost of solving the linear adjoint equations. We expect that $n_{\text{opt}} \approx n_{\text{load}}$, so that up to leading order the total cost of solving the inverse problem is approximately equal to $2n_{\text{load}} \times n_{\text{Newton}}$ linear solves; that is, *it is equal to the cost of solving two forward problems*. This makes our strategy remarkably efficient and competitive with other approaches proposed for solving optimization problems constrained by nonlinear partial differential equations (see, for example [32]). Finally, in the numerical examples considered in this paper the domain of the problem is a rectangle, the initial material parameter distribution is homogeneous, and the boundary conditions are regular. In this special case, the fully loaded nonlinear forward solution required during the first step of the optimization algorithm can be evaluated analytically, or by solving simple nonlinear ODEs with two to three degrees of freedom. This reduces the total cost of solving the inverse problem to $(n_{\text{opt}} - 1) \times n_{\text{Newton}} + n_{\text{opt}}$ linear solves, and with $n_{\text{opt}} \approx n_{\text{load}}$; that is, *the total cost of solving the inverse hyperelasticity problem is roughly equal to the cost of solving the forward hyperelasticity problem*.

5. Numerical examples

In this section, we present two-dimensional examples in which we reconstruct the distribution of nonlinear properties from noisy synthetic displacement fields. The synthetic displacement fields are calculated using a specified distribution of material properties (corresponding to one or more stiff circular inclusions in a homogeneous background) by solving the forward hyperelasticity problem. Thereafter the white Gaussian noise is added to the displacement fields by utilizing the AWGN function in Matlab.

We recover the material properties using only the vertical component (also referred to as the axial component) of the displacement field. This is done to account for the fact that in an elasticity imaging experiment, the horizontal displacement component (lateral to the transducer) is typically too noisy to be useful. We start with a homogeneous guess for the

material property distribution and improve it by using quasi-Newton updates. In particular, we use the BFGS algorithm implemented in the TAO toolkit [33]. We evaluate the gradient of the objective function using the adjoint method as described in section 4.1, and the continuation strategy described in section 4.2. All problems are solved on a uniform 40×40 element mesh with bilinear finite element interpolation functions for both the displacement and material property fields. The results presented are obtained on a single 1.4 GHz Itanium 2 processor. The inverse Neo–Hookean problem takes about 45 min to solve and the Veronda–Westman problem takes about twice as long because it employs two measurements and as a result incurs about two times the cost per iteration.

5.1. Compressible Neo–Hookean material in plane strain

In the first example, we consider a compressible Neo–Hookean material in plane strain. In its incompressible form this material model has been used extensively for rubber-like materials (see [25], for example). It does not display any material nonlinearity and is a straightforward extension of a linear elastic solid to the large deformation regime. We have selected this model to test the performance of our algorithm in situations where the deformation is large and yet the material behavior is linear.

5.1.1. Material behavior. The strain energy function corresponding to a compressible Neo–Hookean material in plane strain is given by (see appendix A.1.)

$$W = \frac{\lambda}{4}(I_2 - 1) - \left(\frac{\lambda}{4} + \frac{\mu}{2}\right) \ln I_2 + \frac{\mu}{2}(I_1 - 2). \quad (38)$$

In the relation above, $I_1 = \text{trace}(\mathbf{C})$ and $I_2 = \det \mathbf{C}$ are the principal invariants of the two-dimensional Cauchy–Green strain tensor \mathbf{C} . Further μ , which is the property we attempt to reconstruct, plays the role of the shear modulus, while λ determines the compressibility of the material. In the example, we have assumed that λ is spatially homogeneous and known *a priori* ($\lambda = 2.5$), while μ is inhomogeneous and unknown. As a result in solving the inverse problem we recover the distribution of μ (starting from a homogeneous guess), while keeping λ fixed at the known value. The target distribution of μ is plotted in figure 3(a). It consists of a hard, cylindrical inclusion imbedded in a softer background.

The second Piola–Kirchhoff stress tensor is derived using (1) and the strain energy density function (38). It is given by

$$S_{IJ} = \frac{\lambda}{2}(I_2 - 1)C_{IJ}^{-1} + \mu(\delta_{IJ} - C_{IJ}^{-1}). \quad (39)$$

The material tangent tensor (11) is given by

$$\mathbb{C}_{IJKL} = (\lambda(I_2 - 1) - 2\mu)\mathbb{B}_{IJKL} + \lambda I_2 C_{IJ}^{-1} C_{KL}^{-1}, \quad (40)$$

where

$$\mathbb{B}_{IJKL} = -\frac{C_{IK}^{-1}C_{JL}^{-1} + C_{IL}^{-1}C_{JK}^{-1}}{2}. \quad (41)$$

Note that for small strains ($\mathbf{C} \approx \mathbf{1}$) the fourth-order material tangent tensor reduces to the linear elasticity tensor for an isotropic material, where μ and λ are identified as the Lamé parameters. In our example by requiring that $\lambda \approx \mu$, we have ensured that the material is compressible and that standard bilinear finite elements can be used to discretize the problem without mesh-locking.

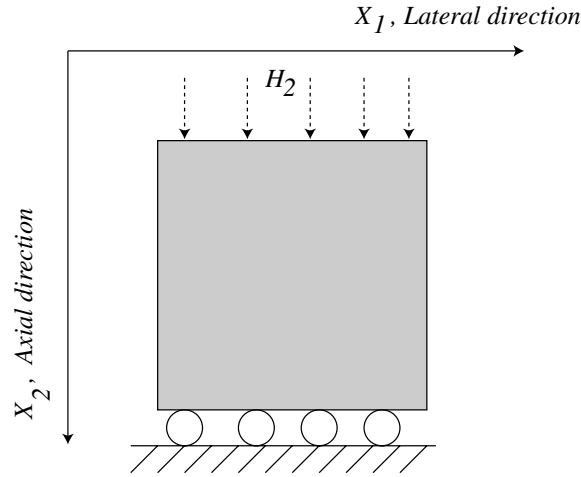


Figure 2. Schematic for the Neo-Hookean problem.

Table 1. Data for the Neo-Hookean example.

Noise level	Displacement noise, $\eta(U_{\text{meas}2})$	Strain noise, $\eta(U_{\text{meas}2,2})$	Regularization parameter, α	Morozov parameter, C
Low	0.3%	3.5%	1×10^{-4}	2.80
Medium	1.0%	12.2%	3×10^{-4}	0.70
High	3.0%	35.0%	1×10^{-3}	0.61

5.1.2. Problem description and results. A schematic of the problem setup is shown in figure 2. The domain consists of a square whose edges are 10 units long. The vertical edges are traction free, while the bottom edge is fixed in the vertical direction ($U_2 = 0$) and traction free in the horizontal direction. The specimen is loaded by a uniform normal traction applied to the top edge where $H_1 = 0$ and $H_2 = 0.5$. This causes the material to compress with an approximate overall strain of about 15%.

Noisy synthetic displacements are generated by solving the forward problem and then adding noise to the solution. The level of noise, measured both in terms of displacements and strains, is reported in table 1. The noise in displacement is measured by $\eta(U_{\text{meas}2})$ which is given by

$$\eta(U_{\text{meas}2}) = \frac{|\mathbf{v}_2 - \bar{\mathbf{v}}_2|}{|\bar{\mathbf{v}}_2|}. \quad (42)$$

Here, \mathbf{v}_2 is a vector that contains the nodal values of the measured (noisy) vertical displacements and $\bar{\mathbf{v}}_2$ is the vector of noiseless or ideal displacements. In an elasticity imaging experiment, the noise in a system is often quantified in terms of noise in the axial strain defined as $\partial U_{\text{meas}2} / \partial X_2$. The noise in this quantity is measured by $\eta(U_{\text{meas}2,2})$ and is also reported in table 1. The reported values of 5–35% noise are consistent with typical measurements in elasticity imaging (see [11]).

We use only the vertical component of the noisy field to solve for the distribution of the shear modulus. We utilize the BFGS algorithm and at each iteration evaluate the gradient using the approach described in section 4.1. We terminate the algorithm after 90 iterations. This corresponds to the point where the drop in the functional over the last five iterations,

normalized by the functional value at the first iteration becomes small (less than 10^{-4}). We select the regularization parameter based on Morozov's discrepancy principle [34]. That is, we choose a value such that the difference between the predicted displacement field and the measured (noisy) displacement field is approximately equal to the difference between the ideal (noiseless) displacement field and the measured displacement field. This ratio is represented in terms of a parameter C given by

$$C = \frac{\|U_2 - U_{\text{meas}2}\|_0}{\|\bar{U}_{\text{meas}2} - U_{\text{meas}2}\|_0}, \quad (43)$$

where U_2 , $U_{\text{meas}2}$ and $\bar{U}_{\text{meas}2}$ are the vertical components of the predicted, the measured and the ideal displacement fields. The regularization parameter is chosen so that $C \approx 1$. Note that in cases where the ideal displacement field is not known the constant C can still be evaluated by replacing the denominator in the above expression by $\eta\|U_{\text{meas}2}\|$, where η is an estimate of the noise. The value of the regularization parameter and the corresponding value of the parameter C are listed in table 1. We note that the regularization parameter increases linearly with the level of noise.

In figure 3, we have plotted the target and reconstructed distributions of μ . We observe that the inclusion is clearly captured in all three cases, and that its boundary is the sharpest when the noise is the least. In figure 4, we have plotted the value of property μ along a horizontal line running through the center. We observe that contrast of the inclusion is accurately recovered in all cases. The value for the reconstructions at lower noise levels are remarkably close to the right answer (1 : 3.8 with medium noise and 1 : 3.9 with low noise).

5.2. Incompressible Veronda–Westman material in plane stress

In the second example, we consider an incompressible material with a nonlinear stress–strain relationship in the state of plane stress. The assumption of plane stress implies that the material is effectively compressible in two dimensions and allows us to use standard bilinear finite elements for modeling it.

5.2.1. Material behavior. In considering the nonlinear behavior of tissue there are several hyperelastic constitutive relations that might be used. These include the Arruda–Boyce model [35] which is motivated by tissue microstructure, the Mooney–Rivlin model (see [25], for example), which may be viewed as an extension of the Neo–Hookean model to higher polynomial orders of strain dependence and the Veronda–Westman model [36], which exhibits an exponential growth of stress with strain. The Veronda–Westman model was originally introduced in [36] to characterize the observed exponential stiffening of soft tissue with applied strain. Besides being an appropriate model for soft tissue behavior, it has the attractive feature that it describes nonlinear behavior with just two independent parameters. This small number of material parameters compared to other models improves the conditioning of the Veronda–Westman inverse problem.

The strain energy density function for an incompressible Veronda–Westman material in the state of plane stress is given by (see appendix A.2)

$$W = \mu \left(\frac{e^{\gamma K_1} - 1}{\gamma} - \frac{K_2}{2} \right), \quad (44)$$

Here, $K_1 = I_1 + 1/I_2 - 3$ and $K_2 = I_2 + I_1/I_2 - 3$. As before, I_1 and I_2 are the principal invariants of the two-dimensional Cauchy–Green strain tensor. Further μ is the shear modulus

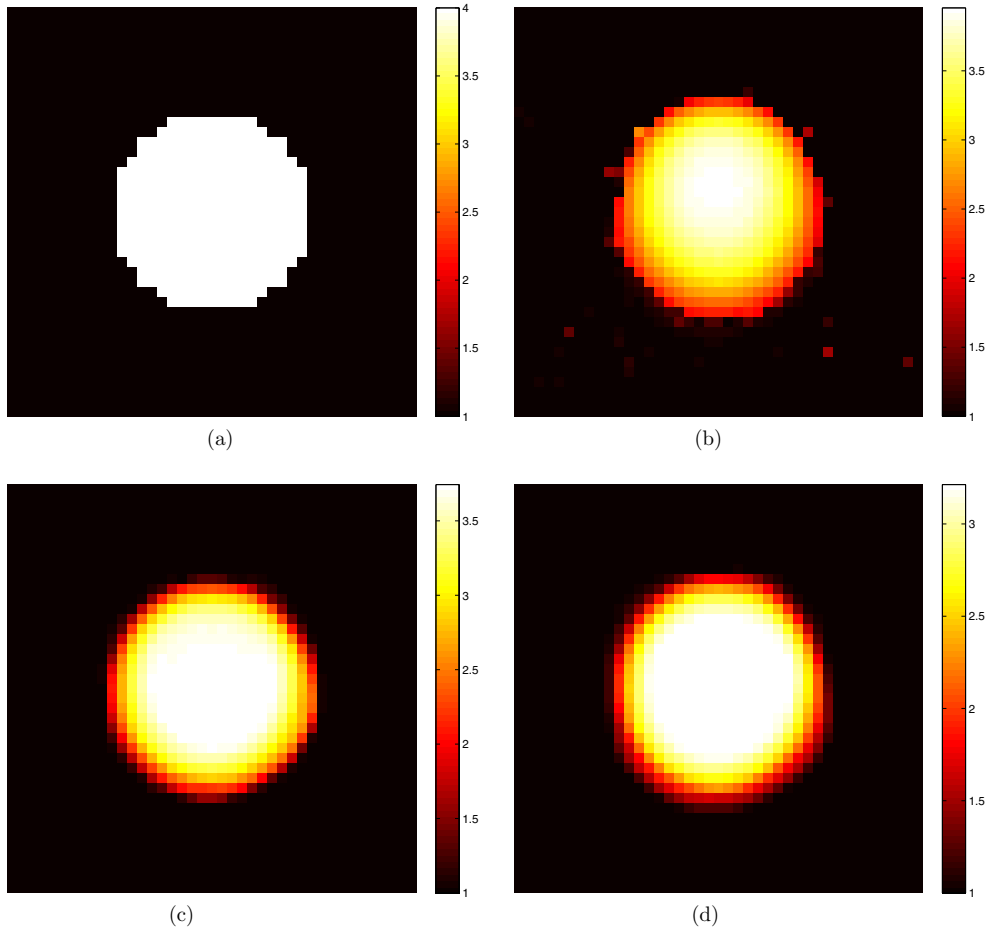


Figure 3. Shear modulus (μ) reconstructions for the Neo-Hookean material: (a) target field, (b) low noise level, (c) medium noise level and (d) high noise level.

of the material at zero strain and γ represents its degree of nonlinearity. The second Piola-Kirchhoff stress tensor is derived from (1) and is given by

$$S_{IJ} = \mu \left(2e^{\gamma K_1} \frac{\partial K_1}{\partial C_{IJ}} - \frac{\partial K_2}{\partial C_{IJ}} \right), \quad (45)$$

where

$$\frac{\partial K_1}{\partial C_{IJ}} = \delta_{IJ} - \frac{C_{IJ}^{-1}}{I_2}, \quad (46)$$

$$\frac{\partial K_2}{\partial C_{IJ}} = \frac{\delta_{IJ}}{I_2} + \left(I_2 - \frac{I_1}{I_2} \right) C_{IJ}^{-1}. \quad (47)$$

Note that in this expression the pressure has been eliminated by assuming a state of plane stress, that is $S_{3I} = 0$ (see appendix A.2). As a result the material behaves like a compressible material in two dimensions. The material tangent is given by

$$\mathbb{C}_{IJKL} = 2\mu \left[2e^{\gamma K_1} \left(\gamma \frac{\partial K_1}{\partial C_{IJ}} \frac{\partial K_1}{\partial C_{KL}} + \frac{\partial^2 K_1}{\partial C_{IJ} \partial C_{KL}} \right) - \frac{\partial^2 K_2}{\partial C_{IJ} \partial C_{KL}} \right], \quad (48)$$

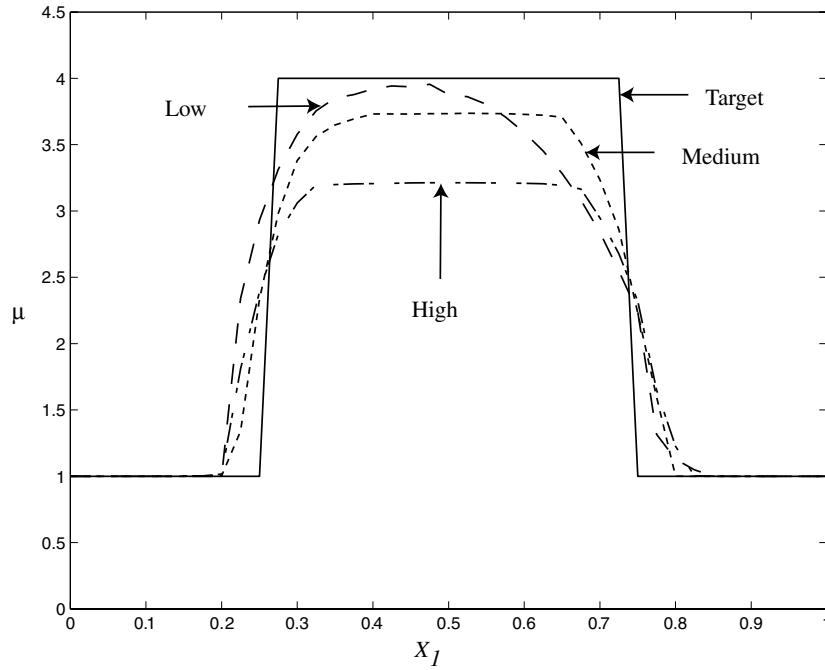


Figure 4. Shear modulus (μ) distribution along a horizontal line through the center.

where

$$\frac{\partial^2 K_1}{\partial C_{IJ} \partial C_{KL}} = \frac{C_{IJ}^{-1} C_{KL}^{-1} - \mathbb{B}_{IJKL}}{I_2} \quad (49)$$

$$\frac{\partial^2 K_2}{\partial C_{IJ} \partial C_{KL}} = \left(I_2 + \frac{I_1}{I_2} \right) C_{IJ}^{-1} C_{KL}^{-1} - \frac{C_{IJ}^{-1} \delta_{KL} + C_{KL}^{-1} \delta_{IJ}}{I_2} + \left(I_2 - \frac{I_1}{I_2} \right) \mathbb{B}_{IJKL}. \quad (50)$$

Evaluating the material tangent at small strains ($\mathbf{C} \approx \mathbf{1}$) gives us

$$\mathbb{C}_{IJKL} \approx 2\mu \delta_{IJ} \delta_{KL} + \mu (\delta_{IK} \delta_{JL} + \delta_{IL} \delta_{JK}). \quad (51)$$

Thus at small strains, this gives the plane stress behavior of a linear elastic incompressible material. Equivalently, this may be thought of as the plane strain behavior of a compressible material with a Poisson's ratio of 1/3. Thus, standard bilinear finite elements perform well for this problem. Further we note that equation (51) shows that at small strains, γ plays no role in determining the stiffness, while μ is the shear modulus. Thus at small strains the response of the material is completely determined by μ . As a result, in order to recover both μ and γ , we require two deformation fields at least one of which must be at sufficiently large overall strain values.

5.2.2. Problem description and results. A schematic of the problem setup is shown in figure 5. The domain consists of a square whose edges are 10 units long. As in the previous example, the vertical edges are traction free while the bottom edge is fixed in the vertical direction ($U_2 = 0$) and traction free in the horizontal direction. The specimen is loaded via a displacement applied to the top edge where $H_1 = 0$ and $U_2 = 0.025$ for the small strain

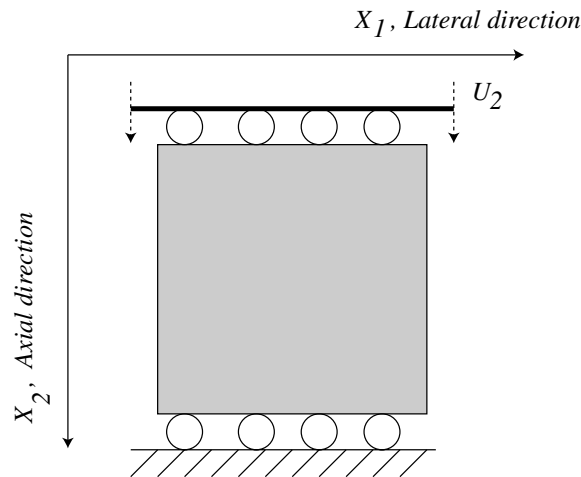


Figure 5. Schematic of the Veronda–Westman problem.

Table 2. Data for the Veronda–Westman example.

Noise level	Displacement $\eta(U_{\text{meas}2})$	Strain noise, noise, $\eta(U_{\text{meas}2,2})$	Regularization parameter, α	Morozov parameter, C
Low	0.3%, 0.3%	3.5%, 3.5%	1×10^{-4}	0.68, 1.17
Medium	1.0%, 1.0%	12.2%, 12.2%	3×10^{-4}	0.60, 0.72
High	3.0%, 3.0%	35.0%, 35.0%	1×10^{-3}	0.54, 0.59

case and $H_1 = 0$ and $U_2 = 2.0$ for the large strain case. This causes the material to compress to an approximate overall strain of about 0.25% and 20% in the small and large strain cases, respectively.

We perform reconstructions at three levels of noise which are reported in table 2. Here for each reconstruction, we have listed the noise in the small strain field first, followed by the noise in the large strain field. The relative noise in both these fields is identical up to the precision of the data.

We use only the vertical component of the noisy displacement fields to solve for the distribution of the shear modulus μ and the nonlinear parameter γ . Since the small strain displacements are much smaller than their large strain counterparts (by a factor of 80), their unweighted effect in the functional would be overwhelmed by the larger displacements. Therefore, we choose the weighting factors in equation (16) to be $w_1 = 80^2$, $w_2 = 1$, where w_1 weights the small-strain displacements. We terminate the BFGS algorithm after 90 iterations. At this point the drop in the functional over the last five iterations, normalized by the functional value at the first iteration becomes smaller than 10^{-3} . Note that for Veronda–Westman we have two regularization parameters: one for μ and another for γ . We have found that the typical sensitivity of the functional to the nonlinear material parameter γ is small. It is approximately 100 times smaller than the sensitivity with respect to μ . Correspondingly, the regularization parameter associated with this variable also has to be smaller. Motivated by this observation we have decided not to regularize γ . The resulting images for γ are rough and we have found that regularizing γ does make them smoother. However, the contrast suffers. Therefore, based on this and our observation about the lower sensitivity to γ , we set the regularization for γ to zero and select the regularization for μ using Morozov's principle.

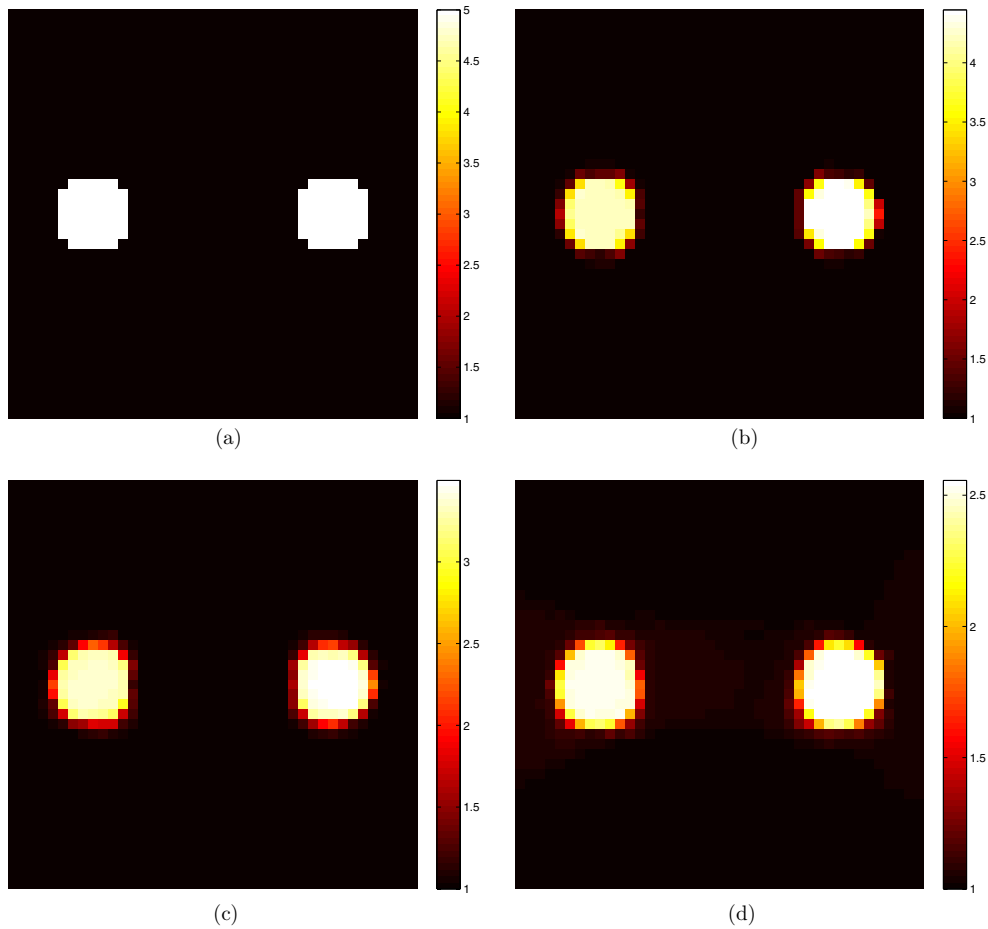


Figure 6. Shear modulus (μ) reconstructions for the Veronda–Westman material: (a) target field, (b) low noise level, (c) medium noise level and (d) high noise level.

Further, since we are matching two displacement fields, there are two values of the Morozov parameter to report. These values along with the values of the regularization parameters appear in table 2. We note that the regularization parameters are identical to the Neo–Hookean case and that the Morozov parameter is uniformly close to unity.

In figures 6 and 8, we have plotted the target and reconstructed distributions of μ and γ . The specimen consists of three inclusions in a homogeneous background with $\mu = 1$ and $\gamma = 1$. Relative to the background all the inclusions harden with strain ($\gamma > 0$). The inclusion on the left has $\mu = 5$ and $\gamma = 3$, and displays the weakest nonlinear behavior. The one in the center has the same shear modulus at zero strain as the background ($\mu = 1$) but is very strongly nonlinear with $\gamma = 10$. The inclusion on the right side has $\mu = 5$ and $\gamma = 8$.

Figure 6 shows the distribution of μ recovered at the three noise levels. In figure 7 we have plotted the value of μ along a line passing through the center of the specimen. We observe that the accuracy of the contrast is inversely related to the level of noise and varies from 50% to about 80%.

In figure 8 we have plotted the distribution of the nonlinear parameter γ at three different noise levels. We observe that the recovered distribution of γ is not as accurate as for μ . In

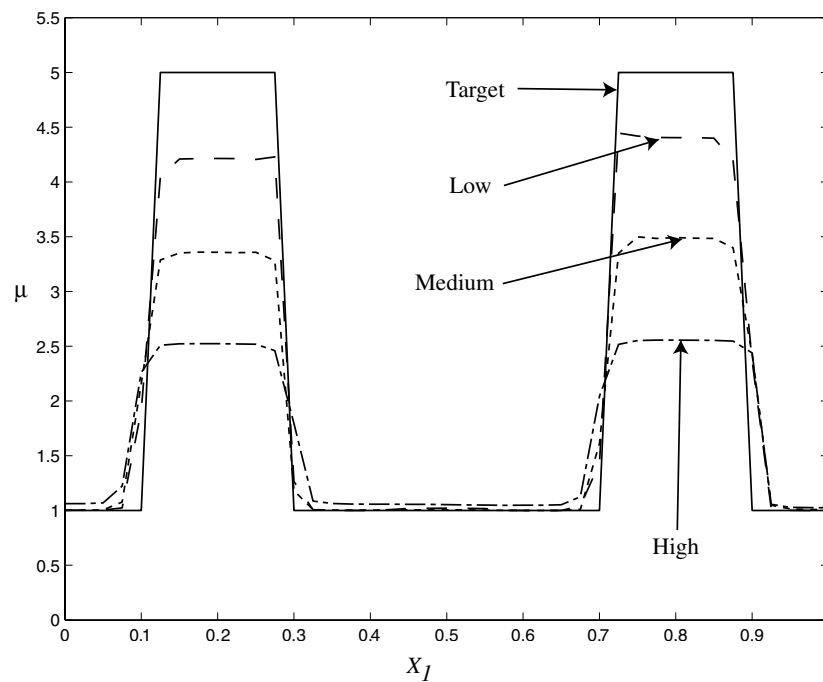


Figure 7. Shear modulus (μ) distribution along a horizontal line through the center for the Veronda–Westman material.

particular, while the central inclusion is clearly observed at all noise levels, the inclusions closer to the edges are not as clear. This is clearly seen in a plot of γ through the center of the inclusions, figure 9. We observe that the contrast for the inclusion on the right is dramatically underpredicted, while the contrast of the central inclusion is more accurate. This discrepancy may be explained by examining the shear modulus at zero strain for these inclusions.

The reconstruction accuracy of the nonlinear parameters depends upon the contrast in the linear stiffness. We can explain this by considering the stress–strain behavior for small strains. For uniaxial stress of an incompressible, Veronda–Westman, material at small strains, we may write

$$\sigma = \underbrace{3\mu\epsilon}_{\text{linear stress}} + \underbrace{3\mu\epsilon^2}_{\text{geometric nonlinearity}} + \underbrace{C\mu\epsilon^3}_{\text{material nonlinearity}} + O(\epsilon^4). \quad (52)$$

Here, σ is the nonzero component of the Cauchy stress, $\epsilon (= \Delta L/L)$ is the nominal (linearized) strain in the direction of the applied stress, μ is the zero-strain shear modulus and $C = 18\gamma - 2$ is a material constant that depends upon γ , the material nonlinearity coefficient in the Veronda–Westman model.

In the presence of measurement error, the strain in (52) will be corrupted by noise. Thus we replace ϵ by $\epsilon + \text{noise}$ in (52), and assuming that noise is small, obtain

$$\sigma \approx 3\mu(\epsilon + \epsilon^2 + \text{noise}) + C\mu\epsilon^3. \quad (53)$$

For the effects of the nonlinear stiffening to be apparent above the noise in the measurement, equation (53) implies that we need

$$|C\epsilon^3| \gtrsim 3|\text{noise}|. \quad (54)$$

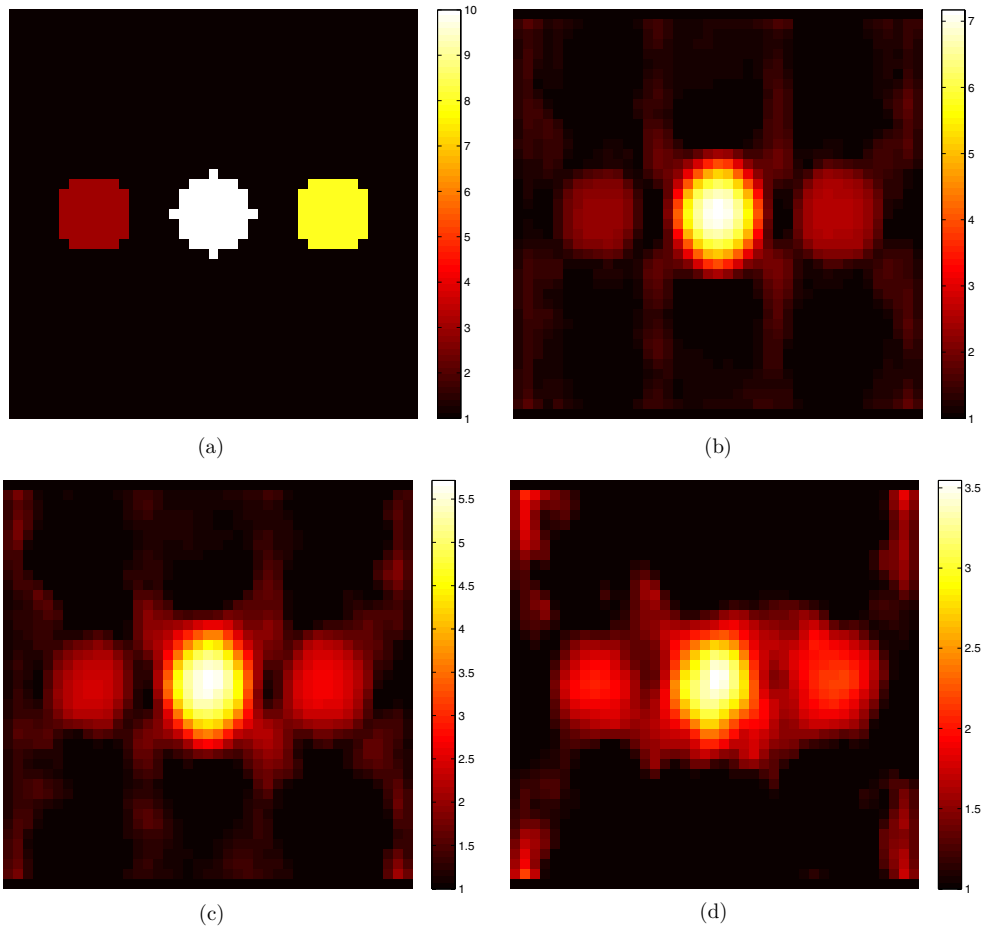


Figure 8. Nonlinear parameter (γ) reconstructions for the Veronda–Westman material: (a) target field, (b) low noise level, (c) medium noise level and (d) high noise level.

We may (crudely) estimate the magnitude of strain in an inclusion to be $\epsilon = \epsilon_0(\mu_0/\mu)$, where μ_0 is the shear modulus in the background, μ is the shear modulus in the inclusion and ϵ_0 is the ‘overall’ applied strain. We may estimate the magnitude of the noise as $|\text{noise}| = \mathcal{N}\epsilon$, where \mathcal{N} is the strain noise level relative to the strain in the inclusion. Substituting these into (54) gives

$$C(\mu_0/\mu)^2\epsilon_0^2 \gtrsim 3\mathcal{N}. \quad (55)$$

Rearranging and using $C = 18\gamma - 2$ gives

$$\epsilon_0^2 \gtrsim \frac{3\mathcal{N}(\mu/\mu_0)^2}{(18\gamma - 2)}. \quad (56)$$

For overall applied strains ϵ_0 that satisfy (56), the nonlinear stiffening would be measurable above the noise. If (56) is not satisfied, then the nonlinear stiffening would not be significant above the noise. These calculations predict that the nonlinear stiffening would be detectable at all noise levels for the central inclusion, barely detectable only at the lowest noise level for

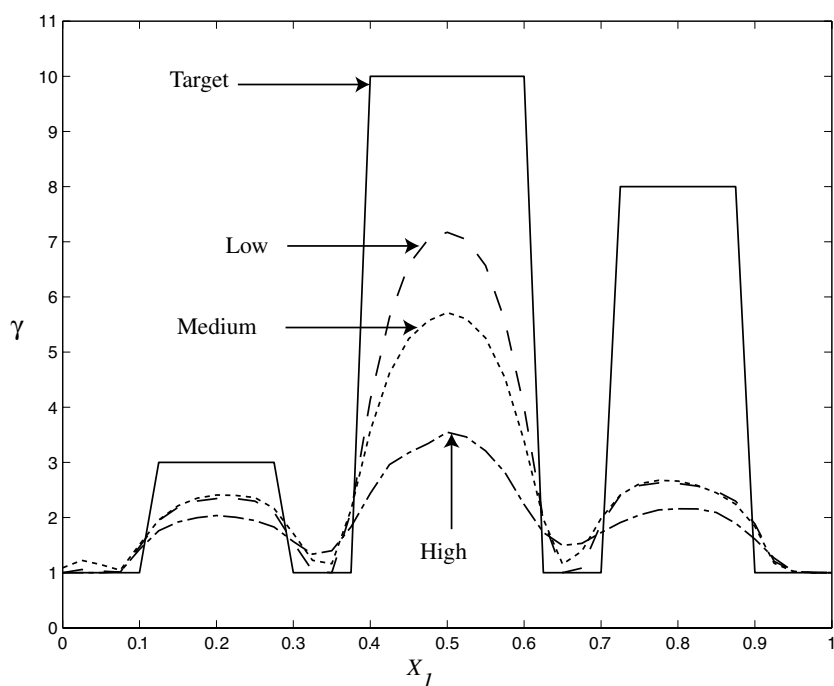


Figure 9. Nonlinear parameter (γ) distribution along a horizontal line through the center for the Veronda–Westman material.

the left inclusion, and detectable at the lower two noise levels for the right inclusion. Thus this analysis qualitatively explains figure 8, but fails to explain why the left and right inclusions are reconstructed with approximately the same γ .

From figure 6, we observe that the shear modulus for the central inclusion is equal to the background, while that of the inclusion to the right is five times higher. Thus the inclusion in the center goes from being as soft as the background at small strains to much stiffer at large strains, while the one to the right goes from being much stiffer to even more stiffer. For the former, we can expect a significant change in the strain pattern in going from small to large strains. At small strains the ratio of strain within the inclusion to the strain in the background is close to unity, while at large strains this ratio is very close to zero. This difference in signal across varying strain levels is sufficiently large when compared to the noise, and the inverse algorithm is able to discern the contrast in the nonlinear parameter. On the other hand, for the inclusion to the right the ratio of the strain within the inclusion to the strain in the background is close to 0.2 at small strains and with increasing overall strain (as the modulus contrast increases) this ratio tends to zero. Hence the difference in signal in moving from small strains to large strains is much smaller in this case. It is likely that this difference is in the range of the noise so that the inverse algorithm is unable to determine the nonlinear parameter accurately.

Efficiency of the continuation strategy. For the Neo–Hookean and Veronda–Westman problems, we commence the solution with a homogeneous guess for the material properties. Due to this, and due to the simplicity of the boundary conditions, we are able to solve the forward problem analytically in the very first iteration of the inverse algorithm. Thereafter

at every iteration, by utilizing the material property continuation strategy, we start from the fully converged solution of the previous iteration and apply the total deformation in a single step. Hence we need typically a total of six Newton iterations to converge to the new forward solution. On the other hand, if we did not rely on the continuation strategy, we would have solved the forward problem at every iteration by applying the total deformation in about 80 steps ($n_{\text{load}} = 80$) and using 6 Newton iterations at each step. Thus the continuation strategy reduces the overall cost by a factor of 80, hence making the solution feasible. Note that the cost of solving the adjoint equations is small when compared with the total cost because these equations are linear.

6. Conclusions

We have considered the problem of determining the nonlinear elastic property distributions of a material undergoing finite deformation from its internal displacement fields. This problem has applications in the field of elasticity imaging, where these material properties may be used to distinguish malignant tissue from benign tissue. We have formulated this inverse problem as a minimization problem where the functional to be minimized measures the difference between the measured and predicted displacement fields. The latter are constrained to satisfy the equations of equilibrium corresponding to a hyperelastic solid. Thereafter, we have presented an efficient approach to solving this problem.

Our approach relies on two strategies which make the solution of this challenging problem feasible. The first involves the use of the adjoint of the linearized hyperelastic equations in order to evaluate the gradient of the functional with respect to the material properties. The second is a continuation strategy which ameliorates the cost associated with solving the nonlinear forward hyperelastic problem at each iteration of the minimization algorithm.

We have applied our approach to cases where the deformation fields are large (15–20% overall strain) and where the material response is nonlinear. We have also assessed its performance in the presence of noise and concluded that at typical noise levels observed in experiments it yields useful results. In this initial development, we have restricted our attention to materials that are effectively compressible in two dimensions. In the context of determining the modulus distribution of tissues this case includes the deformation of incompressible material in the state of plane stress. The extension of this approach to incompressible materials in plane strain and in three dimensions is currently underway and will be addressed in a future article.

Acknowledgments

This work was supported by an award from the DOD Breast Cancer Research Program (Award No. W81XWh-04-1-0763). One of the authors (PEB) acknowledges the support of CenSSIS (The Center for Subsurface Sensing and Imaging Systems) under the Engineering Research Centers Program of the National Science Foundation (Award No. EEC-9986821). In this paper, we have used PETSc [37] for solving systems of linear equations and TAO [33] (Toolkit for Advanced Optimization) library to perform the quasi-Newton optimization.

Appendix. Strain energy functions in two dimensions

In this section we demonstrate that the components of second Piola–Kirchhoff stress tensor for a compressible Neo–Hookean material in plane strain and an incompressible

Veronda–Westman material in plane stress are given by

$$S_{IJ} = 2 \frac{\partial W}{\partial C_{IJ}}, \quad (\text{A.1})$$

for $I, J = 1, 2$. Here, W is the corresponding strain energy function that depends on the two principal invariants (I_1, I_2) of the two-dimensional Cauchy–Green strain tensor.

A.1. The Neo–Hookean material in plane strain

The strain energy function for a compressible Neo–Hookean material in three dimensions is given by (see, for example [25])

$$\bar{W} = \frac{\lambda}{4}(\bar{I}_3 - 1) - \left(\frac{\lambda}{4} + \frac{\mu}{2}\right) \ln \bar{I}_3 + \frac{\mu}{2}(\bar{I}_1 - 3), \quad (\text{A.2})$$

where \bar{I}_1 and \bar{I}_3 are the first and third principal invariants of the three-dimensional Cauchy–Green strain tensor \bar{C} . The components of the second Piola–Kirchhoff stress tensor are given by

$$S_{IJ} = 2 \frac{\partial \bar{W}}{\partial C_{IJ}}. \quad (\text{A.3})$$

Plane strain implies that $\phi_i = \phi_i(X_1, X_2)$, $i = 1, 2$ and $\phi_3 = X_3$. This in turn leads to $C_{13} = C_{23} = 0$ and $C_{33} = 1$. Note from symmetry it also follows that $C_{31} = C_{32} = 0$.

Thus from (A.3) for $I, J = 1, 2$, we have

$$S_{IJ}^\dagger = 2 \frac{\partial \bar{W}}{\partial C_{IJ}} \Big|_{C_{13}=C_{23}=0, C_{33}=1} \quad (\text{A.4})$$

which is the same as (A.1) where $W = \bar{W}|_{C_{13}=C_{23}=0, C_{33}=1}$. Using (A.2), this yields

$$W = \frac{\lambda}{4}(I_2 - 1) - \left(\frac{\lambda}{4} + \frac{\mu}{2}\right) \ln I_2 + \frac{\mu}{2}(I_1 - 2), \quad (\text{A.5})$$

where I_1 and I_2 are the first and second principal invariants of the two-dimensional Cauchy–Green strain tensor C .

A.2. The Veronda–Westman material in plane stress

The strain energy function for an incompressible Veronda–Westman material in three dimensions is given by [36]

$$\bar{W} = \mu \left(\frac{1}{\gamma} (e^{\gamma(\bar{I}_1 - 3)} - 1) - \frac{1}{2}(\bar{I}_2 - 3) \right), \quad (\text{A.6})$$

where \bar{I}_1 and \bar{I}_2 are the first and second principal invariants of the three-dimensional Cauchy–Green strain tensor \bar{C} . The components of the second Piola–Kirchhoff stress tensor are given by

$$S_{IJ} = -p C_{IJ}^{-1} + 2 \frac{\partial \bar{W}}{\partial C_{IJ}}, \quad (\text{A.7})$$

where p is the pressure field. The deformation is volume preserving and thus

$$\bar{I}_3 = \det \bar{C} = 1. \quad (\text{A.8})$$

We assume that plane stress implies $\phi_i = \phi_i(X_1, X_2)$, $i = 1, 2$, and $\phi_3 = \phi_3(X_1, X_2, X_3)$. These conditions in conjunction with the incompressibility constraint (A.8) imply

$C_{13} = C_{23} = 0$ and $C_{33} = 1/I_2$, where I_2 is the determinant of the two-dimensional Cauchy–Green strain tensor. Note that since the second Piola–Kirchhoff stress tensor for any isotropic incompressible solid can be expressed as $\mathbf{S} = -p\mathbf{C}^{-1} + \alpha_1\mathbf{1} + \alpha_2\mathbf{C}$, these conditions ensure that $S_{13} = S_{23} = 0$. In addition we assume that $S_{33} = 0$. This assumption in conjunction with (A.7) and $C_{33} = 1/I_2$ yields an expression for the pressure

$$p = \frac{2}{I_2} \frac{\partial \bar{W}}{\partial C_{33}}. \quad (\text{A.9})$$

From (A.7) for $I, J = 1, 2$, we have

$$S_{IJ} = \left(-pC_{IJ}^{-1} + 2 \frac{\partial \bar{W}}{\partial C_{IJ}} \right) \Big|_{C_{13}=C_{23}=0, C_{33}=1/I_2}. \quad (\text{A.10})$$

Using (A.9) for pressure in the above relation and recognizing that $\frac{\partial I_2}{\partial C_{IJ}} = I_2 C_{IJ}^{-1}$, we conclude that S_{IJ} is given by (A.1) where $W = \bar{W}|_{C_{13}=C_{23}=0, C_{33}=1/I_2}$. Using (A.6), this yields

$$W = \mu \left(\frac{1}{\gamma} (e^{\gamma(I_1+1/I_2-3)} - 1) - \frac{1}{2}(I_2 + I_1/I_2 - 3) \right). \quad (\text{A.11})$$

References

- [1] Ophir J, Cespedes I, Ponnekanti H, Yazdi Y and Li X 1991 Elastography—a quantitative method for imaging the elasticity of biological tissues *Ultrason. Imag.* **13** 111–34
- [2] Figueroa C A, Baek S, Vignon-Clementel I E, Humphrey J D and Taylor C A 2006 Towards patient-specific modeling: I. Hemodynamics in a growing aneurysm *Medical Imaging 2006: Physiology, Function, and Structure from Medical Images* ed A Manduca and A A Amini (*Proc. SPIE* **6143** 186–96)
- [3] Discher D E, Janmey P and Wang Y L 2005 Tissue cells feel and respond to the stiffness of their substrate *Science* **310** 1139–43
- [4] DiMaio S P and Salcudean S E 2003 Needle insertion modelling and simulation *IEEE Trans. Robot. Autom.* **19** 864–75
- [5] Sarvazyan A P, Rudenko O V, Swanson S D, Fowlkes J B and Emelianov S Y 1998 Shear wave elasticity imaging: a new ultrasonic technology of medical diagnostics *Ultrasound Med. Biol.* **24** 1419–35
- [6] Chenevert T L, Skovoroda A R, O'Donnell M and Emelianov S Y 1998 Elasticity reconstructive imaging by means of stimulated echo MRI *Magn. Reson. Med.* **39** 482–90
- [7] O'Donnell M, Skovoroda A R, Shapo B M and Emelianov S Y 1994 Internal displacement and strain imaging using ultrasound speckle tracking *IEEE Trans. Ultrason. Ferroelectr. Freq. Control* **41** 314–25
- [8] Pellot-Barakat C, Frouin F and Insana M 1996 Ultrasound elastography based on multiscale estimations of regularized displacement fields *IEEE Trans. Med. Imaging* **23** 153–63
- [9] Raghavan K R and Yagle A E 1994 Forward and inverse problems in elasticity imaging of soft tissues *IEEE Trans. Nucl. Sci.* **41** 1639–48
- [10] Kallel F and Bertrand M 1996 Tissue elasticity reconstruction using linear perturbation method *IEEE Trans. Med. Imaging* **15** 299–313
- [11] Doyley M M, Meaney P M and Bamber J C 2000 Evaluation of an iterative reconstruction method for quantitative elasticity *Phys. Med. Biol.* **45** 1521–40
- [12] Oberai A A, Gokhale N H and Feijoo G R 2003 Solution of inverse problems in elasticity imaging using the adjoint method *Inverse Problems* **19** 297–313
- [13] Oberai A A, Gokhale N H, Doyley M M and Bamber J C 2004 Evaluation of the adjoint equation based algorithm for elasticity imaging *Phys. Med. Biol.* **49** 2955–74
- [14] Miga M I 2003 A new approach to elastography using mutual information and finite elements *Phys. Med. Biol.* **48** 467–80
- [15] McLaughlin J and Renzi D 2006 Using level set based inversion of arrival times to recover shear wave speed in transient elastography and supersonic imaging *Inverse Problems* **22** 707–25
- [16] Fung Y C 1993 *Biomechanics: Mechanical Properties of Living Tissues* 2nd edn (New York: Springer)
- [17] Wellman P, Howe R H, Dalton E and Kern K A 1999 Breast tissue stiffness in compression is correlated to histological diagnosis *Technical Report* (Harvard BioRobotics Laboratory, Division of Engineering and Applied Sciences, Harvard University)

- [18] Krouskop T A, Wheeler T M, Kallel F, Garra B S and Hall T 1998 Elastic moduli of breast and prostate tissues under compression *Ultrason. Imag.* **20** 260–74
- [19] Gurtin M E *An Introduction to Continuum Mechanics* (New York: Academic)
- [20] Erkamp R Q, Skovoroda A R and O'Donnell M 2002 Nonlinear elasticity imaging *Proc. 2002 IEEE Ultrasonics Symp.* pp 1844–7
- [21] Erkamp R Q, Skovoroda A R, Emelianov S Y and O'Donnell M 2004 Measuring the non-linear elastic properties of tissue like phantoms *IEEE Trans. Ultrason. Ferroelectr. Freq. Control* **51** 410–9
- [22] Erkamp R Q, Emelianov S Y, Skovoroda A R and O'Donnell M 2004 Nonlinear elasticity imaging: theory and phantom study *IEEE Trans. Ultrason. Ferroelectr. Freq. Control* **51** 532–9
- [23] Skovoroda A R, Lubinski M A, Emelianov S Y and O'Donnell M 1999 Reconstructive elasticity imaging for large deformations *IEEE Trans. Ultrason. Ferroelectr. Freq. Control* **46** 523–35
- [24] Marsden J E and Hughes T J R 1983 *Mathematical Foundations of Elasticity* (Englewood Cliffs, NJ: Prentice-Hall)
Marsden J E and Hughes T J R 1994 *Mathematical Foundations of Elasticity* (New York: Dover) (reprinted)
- [25] Simo J C and Hughes T J R 1998 *Computational Inelasticity (Interdisciplinary Applied Mathematics)* (Berlin: Springer)
- [26] Tortorelli D A 1992 Sensitivity analysis for non-linear constrained elastostatic systems *Int. J. Numer. Methods Eng.* **33** 1643–60
- [27] Dorn O, Bertete-Aguirre H, Berryman J G and Papanicolaou G C 1999 A nonlinear inversion method for 3D electromagnetic imaging using adjoint fields *Inverse Problems* **15** 1523–58
- [28] Feijóo G R, Oberai A A and Pinsky P M 2004 An application of shape optimization in the solution of inverse acoustic scattering problems *Inverse Problems* **20** 199–228
- [29] Press W H, Teukolsky S A, Vetterling W T and Flannery B P 1998 *Numerical Recipes in C: The Art of Scientific Computing* 2nd edn (Cambridge: Cambridge University Press)
- [30] Barbone P E and Bamber J C 2002 Quantitative elasticity imaging: what can and cannot be inferred from strain images *Phys. Med. Biol.* **47** 2147–64
- [31] Barbone P E and Gokhale N H 2004 Elastic modulus imaging: on the uniqueness and nonuniqueness of the elastography inverse problem in two dimensions *Inverse Problems* **20** 283–96
- [32] Biros G and Ghattas O 2005 Parallel Lagrange–Newton–Krylov–Schur methods for PDE-constrained optimization: part II. The Lagrange–Newton solver and its application to optimal control of steady viscous flows *SIAM J. Sci. Comput.* **27** 714
- [33] Benson S J, McInnes L C, Moré J and Sarich J 2004 TAO user manual (revision 1.7) *Technical Report ANL/MCS-TM-242* (Mathematics and Computer Science Division, Argonne National Laboratory)
- [34] Vogel C R 2002 *Computational Methods for Inverse Problems* (Philadelphia: SIAM)
- [35] Arruda E M and Boyce M C 1993 A three-dimensional constitutive model for the large stretch behavior of rubber elastic materials *J. Mech. Phys. Solids* **41** 389–412
- [36] Veronda D R and Westman R A 1970 Mechanical characterization of skin—finite deformations *J. Biomech.* **3** 111–22
- [37] Balay S, Gropp W D, McInnes L C and Smith B F 2002 PETSc users manual *Technical Report ANL-95/11—Revision 2.1.3* (Argonne National Laboratory)